ACS OMEGA

http://pubs.acs.org/journal/acsodf

Article

Revaporization Behavior of Cesium and Iodine Compounds from Their Deposits in the Steam−Boron Atmosphere

Muhammad Rizaal,* Shuhei Miwa, Eriko Suzuki, Junpei Imoto, Masahiko Osaka, and Mélany Gouëllo

Cite This: https://doi.org/10.1021/acsomega.1c04441

Read Online

ACCESS | Metrics & More | Article Recommendations | Supporting Information

ABSTRACT: This paper presents our investigation on cesium and iodine revaporization from cesium iodide (CsI) deposits on stainless steel type 304L, which were initiated by boron and/or steam flow. A dedicated basic experimental facility with a thermal gradient tube (TGT) having a temperature range of 1000−400 K was used for simulating the phenomena. In the absence of boron, it was found that the initially deposited CsI at 850 K could be revaporized as CsI vapor/aerosol or reacted with the carrier gas and stainless steel (Cr_2O_3 layer) to form Cs_2CrO_4. The latter mechanism consequently released gaseous iodine that was later accumulated downstream. After introducing boron to the steam flow, a severe revaporization occurred. This, in addition to the revaporized CsI vapor/aerosol, was caused by cesium borate ($Cs_2B_4O_7$ and CsB_5O_8) formation, which then largely released gaseous iodine that was capable of reaching the TGT outlet (<400 K). In the case of a nuclear severe accident, our study has demonstrated that an increase of gaseous iodine in the colder region of a reactor could occur after late release of boron or a subsequent steam flow after refloods of the reactor, thus posing its inherent risk once leaked to the environment.

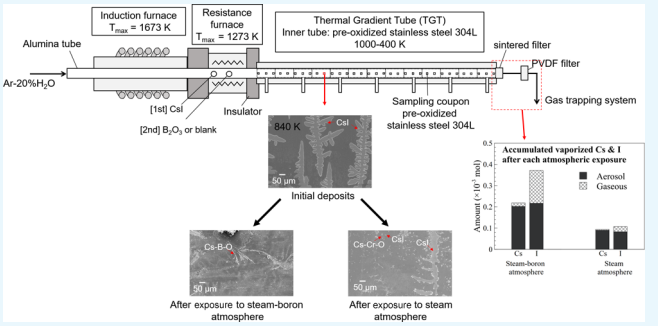

1. INTRODUCTION

The lessons learned from Fukushima Daiichi (1F) nuclear power plant (NPP) severe accident (SA) had brought the importance of more accurate estimations of source term.[1,2] This could be intended for achieving sustained reliability of light water reactor (LWR) safety assessment[3] or understanding fission product (FP) distribution inside the 1F concerning various kinds of decommissioning and dismantling works taken, such as debris retrieval.[2] The source term is defined as the magnitude and the chemical and physical forms of fission product source distribution in the containment atmosphere during the severe accident,[4] which is collectively affected by the accident progression. A thorough understanding and better evaluation of fission products starting from their release behavior from nuclear fuel until their transport behavior in a reactor must be satisfied. Such a kind of comprehension will aid in the use and improvement of SA analysis codes like MELCOR[5] or THALES-2[6] to assess the source term. In the framework of the OECD/NEA BSAF project (Organisation for Economic Co-operation and Development/Nuclear Energy Agency−Benchmark study of the accident at the Fukushima Daiichi NPS), these analytical codes encountered some issues related to FP chemistry due to the inherent complex phenomena and also lack of supporting data for relevant chemical interactions, which at last have induced uncertainties in analyzing the release and transport behaviors of FPs.[7,8] Recognizing the significant impact of the said release and transport behavior of FPs, fundamental research studies on FP chemistry have been initiated in the Japan Atomic Energy Agency (JAEA) encompassing separate- and integral-test experiments.[9−16] The objectives of those research studies are primarily to evaluate FP chemistry and to create and/or improve existing FP chemistry models for database ECUME (Effective Chemistry database of fission products Under Multiphase rEaction).[17,18] The ECUME database consists of three datasets including (1) chemical reaction kinetics, (2) elemental models, and (3) thermodynamic properties, which are implementable in the SA analysis codes. The phenomena and behaviors of FP in ECUME are selected based on the importance and priority for decommissioning work of 1F and safety enhancement of the reactor, where they consist of chemical interaction in the gas phases and gas−condensed phases.

An FP chemistry involving the Cs-I-B-O-H system had been studied in the past in some postulated sequences of the accident to understand the process/mechanism for gaseous iodine generation.[19−22] Suppose a nuclear severe accident in a light water reactor, while taking into account the steam-rich

Received: August 16, 2021
Accepted: November 3, 2021

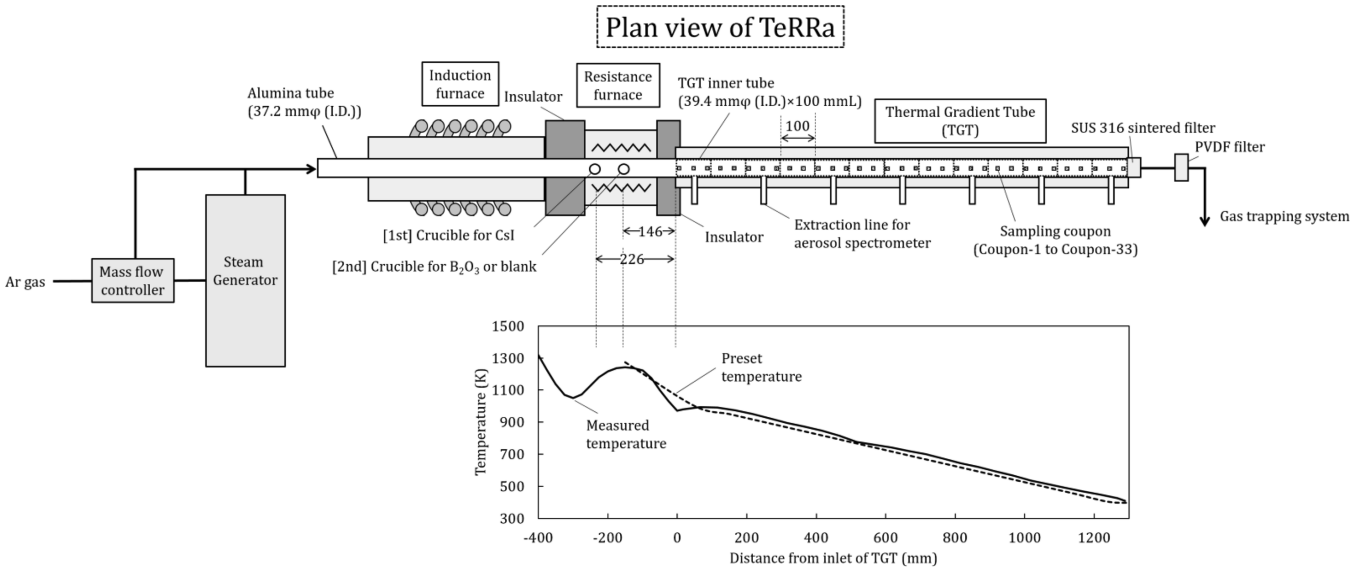

Figure 1. Experimental setup and temperature profile along the furnace and TGT.

condition and temperature lower than 1500 K, the thermodynamic analysis shows that iodine prevails as the CsI (cesium iodide) gaseous phase.[23] This chemical form of iodine remains as CsI even when other elements such as Mo and B are present in the system.[24] Concerning the Cs-I-B-O-H system, the interaction of CsI with boron species would then determine the chemistry of iodine in the reactor. Their interaction could be specified into a homogeneous reaction between the condensed phases[19,22] or gas phases[20] and the heterogeneous reaction of gas-condensed phases.[20,21] Depending on the accident scenario/sequence, the reaction could proceed in any of the conditions. In the gas-condensed phase scenario, the interaction could lead to a revaporization process of CsI deposits.[21] In the previous study by Sato et al.,[21] investigations were focused on the influence of boron-containing Ar gas flow on CsI that was initially deposited on the surface of a vertical tube. They found that boron could strip the deposited CsI at a location with the temperature of 830−920 K. Using thermodynamic calculation, they analyzed the possible formation of gaseous $CsBO_2$ and gaseous iodine after the interaction of CsI and B_2O_3. The authors further evaluated the reaction rate with the presence of O_2 impurity in the carrier gas and concluded that O_2 could control the process even at low partial pressures. Despite the given thermodynamic calculation, there was insufficient evidence on surface analyses that is essential for interpreting the mechanism of interaction. More realistically, B_2O_3 is not the main boron species but boric acids when reflecting the SA condition, where a large amount of steam is present in the system.[25,26] Hence, interaction involving boric acids is more preferred if one considers the revaporization, characterized by a temperature similar to that of the reactor coolant system (<1500 K).

In the present study, we investigate the gas-condensed phase reaction of the Cs-I-B-O-H system using an integral test facility built in JAEA. The test facility called TeRRa (Test-bench for FP Release and tRansport) is designed to reproduce the chemical interaction during FP transport in a severe accident,[10,16] including complex physical and chemical processes of condensation and deposition on the wall of the structural material and aerosol formation/growth as it transits in the reactor coolant system (RCS).[27] TeRRa is equipped with a horizontal thermal gradient tube (TGT) and a set of accompanying analyses of FP behavior for both deposits and aerosol at respective temperature regions in the TGT. The capability of TeRRa to reproduce those complex processes had been demonstrated in the earlier works,[10,16] thus enabling it for further utilization in the present investigation. Through this study, we aim to overcome the knowledge gap of the interaction mechanism among CsI deposits, steam, and boron, and therefore, this could lead to more reliable development of the Cs-I-B-O-H system in the ECUME database.

2. EXPERIMENTAL SECTION

2.1. Experimental Setup. Figure 1 presents a schematic view and basic components of TeRRa. TeRRa consists of two main sections: a section for vaporizing the simulant fission product and a section for analyzing fission product behavior. The former consists of a high-frequency induction furnace and an electric resistance furnace, while the latter consists of a thermal gradient tube (TGT), aerosol spectrometer, and gas trapping system. An alumina tube with an inner diameter of 37.2 mm was installed along the furnace axis and directly connected to thermal gradient tubes with a length of 1300 mm. The TGT has a linear temperature gradient from 1000 to 400 K, which is maintained by individual heaters fixed at interval of 100 mm. In the present study, 13 inner tubes (an inner diameter of 39.4 mm and a length of 100 mm) and 33 sampling coupons (10×10×1 mm; l×w×t) were placed in the TGT. These inner tubes and coupons were made of stainless steel 304L to represent a typical material in the reactor coolant system (RCS) that is highly anticipated to interact with fission products.[12,28] For temperature-dependent analysis, each coupon was located at a specific axial location in TGT and numbered sequentially from the highest temperature location as Coupon-1 up to Coupon-33 at the lowest temperature location. Their exact corresponding temperature was measured using K-type thermocouples in separate heating tests as shown in Figure 1. At the outlet of TGT, a sintered filter made of stainless steel 316 (filtering accuracy below 1 μm) and a polyvinylidene fluoride (PVDF) filter (0.22 μm in pore size, Merck) were installed to collect aerosol generated in the

https://doi.org/10.1021/acsomega.1c04441
ACS Omega XXXX, XXX, XXX−XXX

Table 1. CsI Revaporization Experimental Conditions

	TeRRa-RBS-1 (steam−boron effect)	TeRRa-RBS-2 (steam effect)
deposition phase [1st heating of TeRRa]		
simulant FP material/amount (g)	CsI powder/2.80	CsI powder/2.80
crucible/heating temperature (K)	alumina/1180	alumina/1180
electric resistance furnace temperature (K)	1273	1273
induction furnace temperature (K)	1673	1673
TGT temperature (K)	1000−400	1000−400
TGT inner tube and coupon materials	pre-oxidized stainless steel 304L	pre-oxidized stainless steel 304L
gas composition/inlet temperature (K)/flow rate (L/min)[a]	Ar-20 vol % H_2O/400/2	Ar-20 vol % H_2O/400/2
pressure (MPa)	0.1	0.1
revaporization phase [2nd heating of TeRRa]		
material/amount (g)	B_2O_3 powder/1.40	
crucible/heating temperature (K)	alumina/1273	
electric resistance furnace temperature (K)	1273	1273
induction furnace temperature (K)	1673	1673
TGT temperature (K)	1000−400	1000−400
gas composition/inlet temperature (K)/flow rate (L/min)[a]	Ar-20 vol % H_2O/400/2	Ar-20 vol % H_2O/400/2
pressure (MPa)	0.1	0.1

[a]STP condition: T = 273.15 K; P = 101.325 kPa.

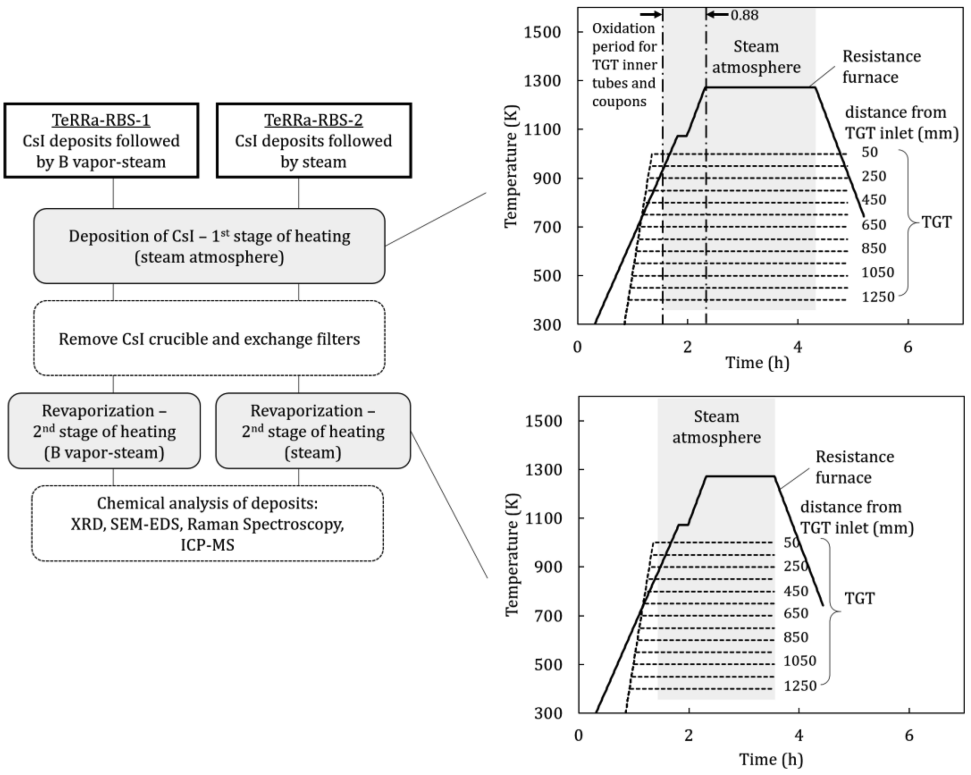

Figure 2. Summary of the overall experimental procedure.

experiments. Additionally, the gas trapping system made of two gas bubbler bottles containing a mixed solution of 0.2 M NaOH and 0.02 M $Na_2S_2O_3$ in which gaseous iodine is intended to be collected was integrated downstream of filters. It should be highlighted that in this study, we regard the iodine passing the filters and collected in the solution of gas bubbler bottles as a gaseous phase and presume that the aerosol has been trapped in the filters.

2.2. Experimental Procedure. The experimental condition employed throughout heating tests of revaporization of CsI is given in Table 1, while Figure 2 presents the summary of the experimental procedure at respective stages. In this study, we investigated the revaporization process initiated by high-temperature steam containing boron (referred to as TeRRa-RBS-1; Revaporization by Boron and/or Steam) and high-temperature steam without boron (referred to as TeRRa-RBS-2) serving as the reference case. Both TeRRa-RBS-1 and TeRRa-RBS-2 are two independent experiments and hence would not influence the characteristics of each experimental result. The procedure described hereinafter is applied for TeRRa-RBS-1 due to the analogous conditions in TeRRa-RBS-2, except for the inclusion of an alumina crucible filled with B_2O_3 powder at the second stage of heating.

https://doi.org/10.1021/acsomega.1c04441
ACS Omega XXXX, XXX, XXX−XXX

Initially, the inner tubes and sampling coupons were set in the TGT, and an alumina crucible (14 × 14 mm; $d \times h$) filled with CsI powder (99.9%, Wako Inc.) was positioned in the resistance furnace at the axial location having a temperature of 1180 K (Figure 1; 226 mm upstream from the TGT). This vaporization temperature was chosen to prevent rapid depletion of CsI in the crucible during the experiment while still keeping the vaporization rate nearly constant. The temperatures in the TGT, resistance furnace, and induction furnace were then increased to the target temperature of 1000 to 400 K (heating rate in each spatial heaters varied in 20−35 K/min), 1273 K (heating rate: 9 K/min), and 1673 K (heating rate: 10 K/min), respectively. During the heating up process, 2 L/min (STP) Ar (O_2 impurity: 1 ppm) gas flow was fed to the alumina tube and became superheated as it transited the induction furnace. Steam would be added to the Ar gas flow by the steam generator with a composition of Ar-20%H_2O (i.e., 19.93 kPa of H_2O partial pressure at 60 °C) when the temperature in the resistance furnace reached 920 K (Figure 2). It should be emphasized that there was 53 min (0.88 h) for steam to pre-oxidize stainless steel inner tubes and coupons in the TGT before achieving the maximum temperature of 1273 K at the resistance furnace. Ishida et al.[29] have confirmed the oxidation behavior of stainless steel 304 under steam within this short period in particular at the first 8 min of the oxidation course, where two oxide layers consisting of Fe and Cr were formed. At this 53 min period, the vaporization of CsI was limited. This means that the inner tubes and coupons in the TGT had been oxidized depending on their axial-wise temperature before the interaction with CsI started. This surface state is important to represent the condition of stainless steel as similar as possible to that in the reactor coolant system after hours of operation in the steam condition or during the severe accident.[30] After 2 h vaporization of CsI under Ar-20% H_2O, the gas flow was then changed to Ar and followed by the cooling process (cooling rate: 10 K/min). The CsI crucible was removed and the filters at the TGT outlet were exchanged. An alumina crucible (14 × 14 mm; $d \times h$) filled with B_2O_3 powder (99.995%, Kojundo Chemical Laboratory Co., Ltd.) was then placed in the resistance furnace at the axial location with a temperature of 1273 K (Figure 1; 146 mm upstream from the TGT). It is worth explaining that in this study, B_2O_3 was still used as a boron source, considering its first potential formation when boron in the mixed melt of B_4C-SS-Zry was oxidized and vaporized.[25,26,31] But when the condition is developed with the presence of steam taken into account, B_2O_3 might be transported as boric acids. Next, the heating process was repeated under the Ar-20%H_2O gas flow and sustained for 1.25 h. After the cooling process, each of the TGT inner tubes and the filters were taken and subjected for mass spectroscopic analysis using inductively coupled plasma−mass spectrometry (ICP-MS). Separately, the sampling coupons were analyzed using scanning electron microscopy/energy dispersive X-ray spectrometry, X-ray diffractometry, and Raman spectrometry. The specific target analysis given by each post-experiment measurement is further explained in the next subsection.

2.3. Post-Test Analyses. The TGT inner tubes and filters used at the first and second stages of heating were immersed in 0.04 M NaOH solution at room temperature for about 18 h. The immersion was intended to remove all the deposits contained on the surface of tubes and filters. The supernatants of those solutions as well as solutions from two bottles of the gas trapping system were further diluted to the appropriate concentrations for the measurement of Cs, I, and/or B amount by ICP-MS (Agilent 8800, Agilent Technology) with the uncertainty of 5% (based on repeated measurement results on reference Cs, I, and B samples).

The microstructure and elemental distribution of deposits formed on sampling coupons were analyzed using scanning electron microscopy equipped with an energy dispersive X-ray spectrometer (SEM/EDS-silicon drift detector, JSM-IT100, JEOL). The accelerating voltage was 10 kV to accommodate the light element analysis of boron.[32,33] X-ray diffractometry (XRD) and Raman spectroscopy were also applied to evaluate the chemical forms of the deposits on coupons. The XRD analysis was performed with a Miniflex600 (Rigaku) X-ray diffractometer at room temperature using Cu-Kα radiation over the scan range of 2θ of 10−80° in continuous mode with a step size of 0.01° and the scanning speed of 1°/min. The applied voltage and current were 40 kV and 15 mA, respectively. The Raman spectra were recorded with an NRS-4500 (JASCO) Raman spectrometer, which utilized the 532 nm line of laser diode (0.3 mW), a grating of 900 grooves/mm, and a 100 μm entrance slit. The spectral range was set from 45 to 3800 cm^{-1} in an exposure time of 10 s with five times accumulation.

3. RESULTS AND DISCUSSION

3.1. Deposition of Cesium, Iodine, and Boron in the Thermal Gradient Tube. The collated mass spectroscopy data on the deposition phase (referred to as TeRRa-CsI)[16] and revaporization affected by steam−boron (TeRRa-RBS-1) and steam (TeRRa-RBS-2) are presented in Figure 3a,b, respectively. The deposition fraction is defined as the ratio of respective elements at a certain location to the total amount of such an element collected in TGTs, filters, and gas trapping. In the deposition phase,[16] a noticeably large amount of Cs and I was deposited in the regions with a temperature range of 870−830 K and 820−780 K. This deposition was a result of cesium iodide condensation (903 K[34]), which is similar to that in the report by Sato et al.,[21] who indicated that the highest deposition occurred in the mid-part of "Area A" in their study (i.e., corresponded to approximately 840−790 K in the vertical tube), and in another report by Hidaka et al.[35] with the study of CsI deposition under a nitrogen gas flow where they observed the highest deposition on coupon nos. 2 and 3 (930−790 K). This suggests that the highest CsI deposition region is independent of the flow direction (vertically or horizontally) and of inert gas or steam once it is deposited. In other words, the underlying process is vapor condensation. However, to some extent, this does not apply when the deposits are subjected to the subsequent high-temperature steam flow (e.g., resulted from refloods of the reactor) or the reheat (resulted from decay heat), which induces a distinct depositional condition.

Two independent revaporization experimental series showed that the initial large deposition on the surface with a mean temperature of 850 K was unstable and apt to vaporize. In TeRRa-RBS-2 (steam effect), Cs and I depositions were 0.219 ± 0.011 and 0.178 ± 0.009 mmol or equivalent to fractions of 0.091 ± 0.005 and 0.074 ± 0.004 (Figure 3b), respectively, while in TeRRa-RBS-1 (steam−boron effect), the Cs and I depositions were 0.238 ± 0.012 and 0.086 ± 0.004 mmol or equivalent to fractions of 0.077 ± 0.004 and 0.029 ± 0.002 (Figure 3a). There were relative reductions of 46.0 ± 6.1% Cs and 50.9 ± 6.1% I deposits in TeRRa-RBS-2 and 41.2 ± 6.2%

https://doi.org/10.1021/acsomega.1c04441
ACS Omega XXXX, XXX, XXX−XXX

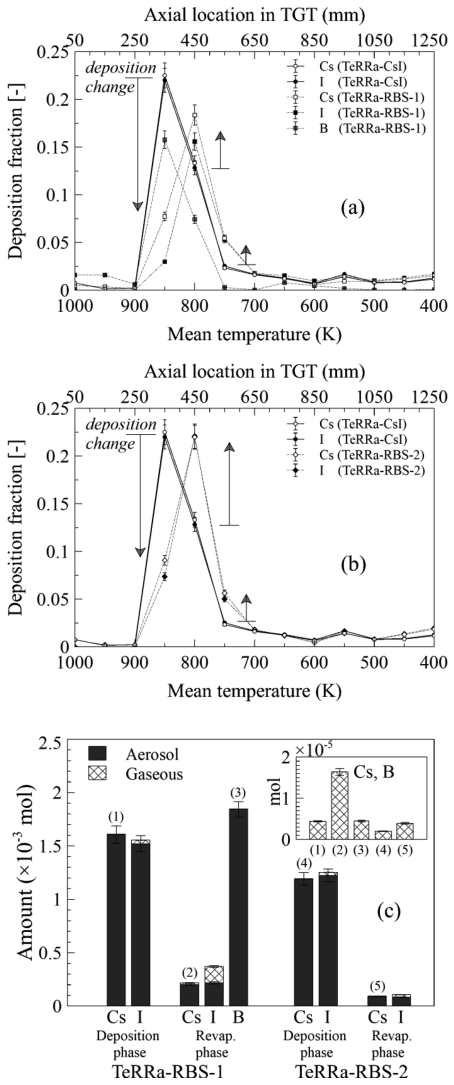

Figure 3. Deposition profile of Cs, I, and B in a thermal gradient tube of test series: (a) TeRRa-CsI (initial deposition[16]) and TeRRa-RBS-1 (steam−boron effect) and (b) TeRRa-CsI and TeRRa-RBS-2 (steam effect). (c) Measured amount of Cs, I, and B reaching the outlet of the thermal gradient tube (T < 400 K).

Cs and 76.1 ± 6.4% I deposits in TeRRa-RBS-1 on stainless steel at this location as compared to TeRRa-CsI (i.e., 0.405 ± 0.020 mmol of Cs and 0.363 ± 0.018 mmol of I), which was then transported downstream. We found that two effects resulted from this vaporization: (1) redeposition on the surface with mean temperatures of 800 and 750 K and (2) generation of secondary aerosol and gaseous iodine (Figure 3c; which were collected at the outlet of TGT with a temperature lower than 400 K). The redeposition on both tests possessed a similar trend with different magnitudes in which more deposition occurred in the steam atmosphere. Given the vapor pressure of the equilibrium CsI(s) = CsI(g) below the melting point[36] as

$$\log p(\text{atm}) = \frac{-9550 \pm 79}{T} + (6.945 \pm 0.093) \quad (1)$$

it is found that the redeposition in the steam atmosphere is affected by the 5-fold decrease of vapor pressure (at 800 K) and thus could induce the formation of condensed CsI. The large deposition of boron at 850 K, however, signifies an interaction with CsI deposits, inasmuch as the separate-effect test with boron (without CsI) showed that the deposition of boron on type-304L stainless steel was very limited on this temperature.[10] Then, it might influence the immediate vaporization of CsI through the alteration in equilibrium vapor pressure. At the lower temperature region (T < 750 K), there were no changes on the deposition profile, suggesting that the saturation condition had occurred over the aerosol formation and its growth to the outlet of the TGT. Aerosol generated in the first stage of heating (Figure 3c; deposition phase) was more abundant than the gaseous form and was associated with the I/Cs molar ratio closer to unity. It is considered that the vaporized CsI at the source location (resistance furnace)—transported downstream by gas flow—had a limited gas−solid chemical interaction with the stainless steel surface or its dissociation to release gaseous iodine. Approximately 2% gaseous iodine obtained in both tests during the deposition phase was related to the uncondensed monomer and dimer of gaseous CsI or reaction of the CsI condensed phase with the chromium oxide layer at the higher temperature region.[16] In the second stage of heating (Figure 3c; revaporization phase) where CsI at the source location was absent, the secondary aerosol and gaseous iodine were generated. The secondary aerosols for both TeRRa-RBS-1 (steam−boron effect) and TeRRa-RBS-2 (steam effect) are proportionally related to the vaporized CsI on 850 K upon subtracting those deposited amounts on 800−750 K (considering negligible deposition below 750 K); meanwhile, the secondary gaseous iodine is due to interactions that occurred involving boron or steam.

The consistency between the collected aerosol at the downstream of TGT and those deposited in a temperature range of 800−750 K was obtained in both tests. Fewer redeposition of aerosol was found in TeRRa-RBS-1 (steam−boron effect) as compared to TeRRa-RBS-2 (steam effect), and this enabled a large amount of aerosol to reach downstream of TGT. On the other hand, only a smaller fraction of aerosol could reach the downstream of TGT in TeRRa-RBS-2 due to extensive aerosol redepositions at 800−750 K. Furthermore, nearly 42% of the total 0.371 ± 0.010 mmol of iodine reaching the outlet of TGT was a gaseous phase in the presence of boron, while the steam case gave 23% of the total 0.107 ± 0.004 mmol of iodine. In the former case, generation of gaseous iodine was considered as the reaction between CsI deposits and boron, which also produced a low volatile cesium borate compound, while the latter might have resulted from the reaction of CsI deposits with the stainless steel that produced gaseous iodine and cesium chromate. At the given temperature (850−750 K), the expected cesium borates and cesium chromate are in the condensed phase,[23,37−39] and hence, their existence as condensate on the stainless steel surface would corroborate the revaporization mechanism (i.e., secondary gaseous iodine generation). Also, at the revaporization phase in TeRRa-RBS-1 (steam−boron effect), it has been confirmed that the iodine aerosol transited to the colder region as CsI with the given molar ratio equal to 1. Thus, cesium at this location is not associated with boron, and this leads to the evidence that the boron aerosol is boric acid[10,40] instead of Cs-B-O (cesium borates) compounds. In the least possibility that the latter could reach the colder region by taking the form of a gaseous phase, its fraction is unlikely to be large enough (Figure 3c; points (2) and (3)) and the

https://doi.org/10.1021/acsomega.1c04441
ACS Omega XXXX, XXX, XXX−XXX

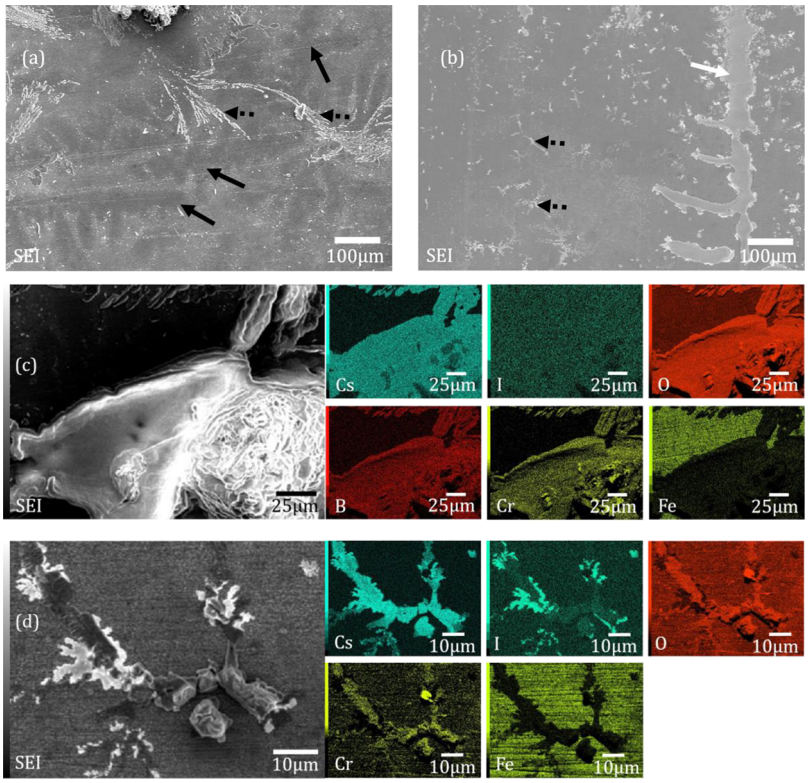

Figure 4. Secondary electron images of Coupon-10 (840 K) in (a) TeRRa-RBS-1 (steam−boron effect) and (b) TeRRa-RBS-2 (steam effect). Solid black arrows indicate the vaporized site of CsI deposits, and dashed black arrows show fine agglomeration, while the white arrow shows the remaining large agglomeration of CsI. Element distribution mapped on the proximity of fine agglomeration in (c) TeRRa-RBS-1 and (d) TeRRa-RBS-2.

chemical compound would be related to the Cs/B ratio closer to 4.

3.2. Compositions and Morphologies of Deposits. Mass spectroscopy analysis in the preceding section had shown that the principal phenomena occurred on the stainless steel surface with a mean temperature of 850 K for the Cs and I revaporization. In addition, the redeposition at 800−750 K as well as at 400 K would also be important concerning the formed chemical compounds.

Figure 4 presents the secondary electron images and the elemental distributions taken from Coupon-10 of TeRRa-RBS-1 and TeRRa-RBS-2, respectively, with the corresponding temperature of 840 K. The vaporized sites are indicated by the solid black arrows in Figure 4a, having the size of submillimeters. This is similar to that of the remaining CsI deposit in Figure 4b shown by the solid white arrow that resulted from agglomeration and solidification upon cooling down of the facility.[16] In TeRRa-RBS-2 (steam effect), these sites were hardly observed yet finer agglomeration appeared. Figure 4d gives the element distribution mapped on the proximity of this fine agglomeration. Cesium and iodine as the heavier elements in the present analysis are shown as bright irregularly shaped particles on the bulk of agglomerates. These particles exist on the boundaries of larger particles, which were suggested by the elemental congruency to have a form of Cs-Cr-O. The configuration of CsI and Cs-Cr-O particles could be explained by the sequence of events in our experimental procedure. Allen et al.[41] showed that a chromium oxide layer was formed on stainless steel under a steam atmosphere at 823 K, and Mamede et al.[30] further confirmed such a formation and highlighted the importance of Cr_2O_3 for a temperature below around 973 K. Therefore, the sequence of interaction could be inferred as follows: First, the Cr_2O_3 layer was formed during the initial heating stage. Second, the CsI vapor was condensed and deposited to cover such a layer. Last, upon the second stage of heating, the CsI deposits that had direct contact on the layer would have a chemical reaction; otherwise, it remained depending on the equilibrium partial pressure. Hence, one might observe a depletion of CsI deposits at this area, progressing from the center toward the edge. The element mapping on the fine agglomerate in TeRRa-RBS-1 (steam−boron effect) is provided in Figure 4c. Unlike TeRRa-RBS-2, Cs-Cr-O elemental distributions (congruently) and Cs-I distribution were scarcely identified, but congruency among Cs-B-O particles became apparent. This indicates that the fine agglomerate is composed of different constituents to those of TeRRa-RBS-2 and turns out as evidence of low volatile cesium borate formation. The spread of this agglomerate (Figure 4a; dashed black arrows) did not resemble the vaporized sites (Figure 4a; solid black arrows) or was separated in distance, which implied that the reaction with boron took place after the condensed CsI had been vaporized from the surface. The volatility of CsI is higher than that in TeRRa-RBS-2 (steam effect) as the addition of boron would reduce the partial pressure of steam. Therefore, it is consistent with the less iodine amount at this location by ICP-MS analysis (Figure 3a). The form of boron at the initial state would exist as condensed B_2O_3 or boric acid vapors (HBO_2, $(HBO_2)_3$, and H_3BO_3) depending on its concentration in the gas flow, i.e., B/H_2O ratio.[10] Then, it would formalize the mechanism of the boron−CsI interaction.

https://doi.org/10.1021/acsomega.1c04441
ACS Omega XXXX, XXX, XXX−XXX

Following the revaporization region with a mean temperature of 850 K, it had been shown from mass spectroscopic analysis in TeRRa-RBS-1 that boron deposition was only noticeable on 820−780 K, while in TeRRa-RBS-2, the Cs-rich location (I/Cs < 1.0) was on 770−730 K. Below these temperature ranges, the I/Cs ratio had been saturated on unity, suggesting no formation or deposition of either Cs-B-O or Cs-Cr-O compounds. Therefore, the analyses have focused on the surface of locations with noticeable B, I/Cs < 1, as well as the location with a temperature of 400 K to represent the lowest preset temperature in TGT. Figure 5 presents the secondary

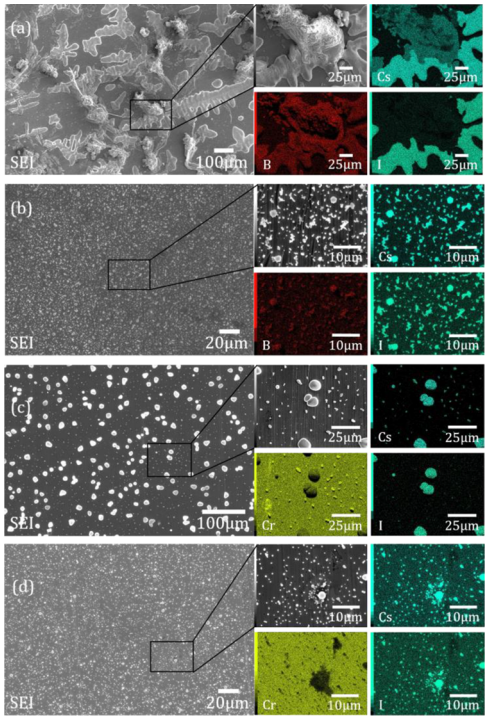

Figure 5. Secondary electron images and element distribution on (a) Coupon-11 (820 K) and (b) Coupon-32 (400 K) of TeRRa-RBS-1 (steam−boron effect) and (c) Coupon-14 (760 K) and (d) Coupon-32 (400 K) of TeRRa-RBS-2 (steam effect). Black rectangles show the mapping area on each coupon.

electron images and the elemental distributions taken from Coupon-11 (820 K) and Coupon-32 (400 K) of TeRRa-RBS-1 and Coupon-14 (760 K) and Coupon-32 (400 K) of TeRRa-RBS-2. On Coupon-11 of TeRRa-RBS-1 (Figure 5a), Cs-B-O particles were found along with large agglomerates consisting of CsI. The presence of Cs-B-O particles on the proximity of CsI agglomerates indicates that the formation of Cs-B-O occurred when the boron vapor and CsI condensed phase were involved. Even though the temperature difference with Coupon-10 (revaporization site) was relatively small, the mechanism of the boron−CsI interaction at this location is quite different. The former has been highlighted by the interaction between boron vapor and CsI vapor (homogeneous reaction), while the latter is signified by an interaction between boron vapor and condensed CsI (heterogeneous reaction). Therefore, in the scope of our experiment, we could confirm that those reactions prevailed inseparably. Despite distinction in reactions, the Raman spectra of those coupons showed similar kinds of Cs-B-O compounds (Figure 6). They are dicesium tetraborate pentahydrate ($Cs_2B_4O_7{\cdot}5H_2O$) and

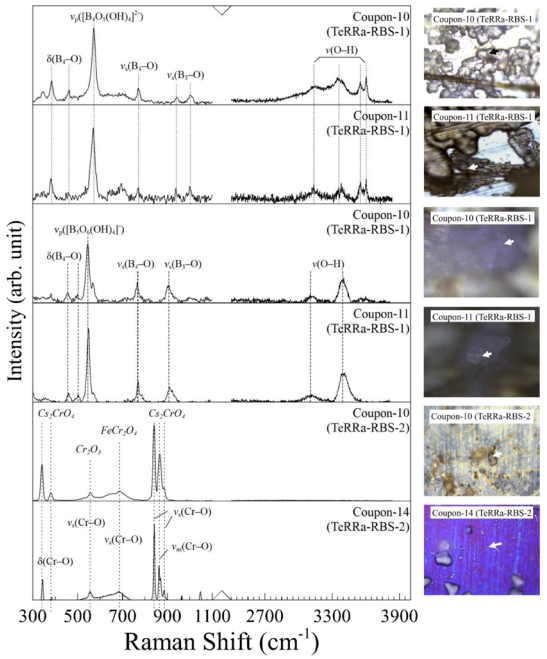

Figure 6. Raman spectra of Coupon-10 and Coupon-11 of TeRRa-RBS-1 and Coupon-10 and Coupon-14 of TeRRa-RBS-2 together with the microscopic images showing the location where the spectra were recorded.

cesium pentaborate tetrahydrate ($CsB_5O_8{\cdot}4H_2O$), as correlated with the reference spectra by Lixia et al.[42] and Zhihong et al.[43] The sharp vibrational bands at 548 and 570 cm^{-1} are assigned to pentaborate anion $[B_5O_6(OH)_4]^-$ and tetraborate anion $[B_4O_5(OH)_4]^{2-}$ stretching modes, respectively, followed by B_4-O symmetric stretching mode (ν_s) at 767 cm^{-1} (pentaborate) and 771 cm^{-1} (tetraborate) and B_3-O symmetric stretching mode at 906 cm^{-1} (pentaborate) and 938 and 1001 cm^{-1} (tetraborate). Vibrational bands at 457 and 500 cm^{-1} (pentaborate) and 461 and 382 cm^{-1} (tetraborate) are attributed to B_4-O bending mode (δ). The O−H stretching modes are assigned to the vibrational bands at 3137 and 3402 cm^{-1} for pentaborate and 3144, 3382, 3553, and 3604 cm^{-1} for tetraborate. Touboul et al.,[44] Penin et al.,[45] and Anderson et al.[46] have demonstrated the thermal behavior of these cesium borates. For details, they showed that the hydrated borates are the stable compounds at the room-temperature condition and that anhydrous $Cs_2B_4O_7$ and α-CsB_5O_8 (or CsB_5O_8 (IV)) are at high temperatures. Thus, in the thermodynamic calculation, the initial formations of these anhydrous compounds are evaluated.

Deposits found on Coupon-32 (Figure 5b) only consisted of CsI, which signified that the cesium borate formation was not favored at low temperatures. Also, the boron-only deposits (as boric acids) could not be identified. This means that the boron vapor/aerosol had a deposition on the colder region as found on filters downstream of TGT (Figure 3c).

At a temperature of 760 K in TeRRa-RBS-2 (steam effect) that is represented by Coupon-14, Cs-Cr-O was identified together with CsI deposits (Figure 5c). The CsI deposits are more spherically shaped with fewer deposits formed by two or more particle agglomerates with an average size of 6 μm. Cs-Cr-O, on the other hand, has lath-like and spherical shapes with a size smaller than 1 μm and spreads without direct contact with CsI deposits. This suggests that Cs-Cr-O was

https://doi.org/10.1021/acsomega.1c04441
ACS Omega XXXX, XXX, XXX−XXX

formed by the interaction of a chromium oxide layer with secondary CsI vapor/aerosol, which resulted from vaporization at the higher temperature location, instead of interaction with the predeposited CsI as observed on Coupon-10 (Figure 4d). Cs-Cr-O on both Coupon-10 and Coupon-11, however, was identified as cesium chromate[47,48] (Cs_2CrO_4) by Raman spectroscopy (Figure 6). It is inferred that the underlying process in both locations (temperatures) is essentially similar. The process would require the condensed phase of CsI with a high specific surface area (i.e., smaller deposits/particles or fine agglomerates) and the preformed chromium oxide layer on stainless steel. The chromium oxide (Cr_2O_3) layers on Coupon-10 and Coupon-11 are identified by the vibrational band at 555 cm^{-1} along with iron(II) chromite $FeCr_2O_4$ by the vibrational band at 684 cm^{-1}.[49] Upon temperature decrease to 400 K, the active vibrational band was only $FeCr_2O_4$. This explains no further formation of cesium chromate despite the existence of small deposits (<1 μm) at 400 K (Figure 5d).

The X-ray diffraction patterns of Coupon-10, Coupon-11, and Coupon-32 for TeRRa-RBS-1 and Coupon-10, Coupon-14, and Coupon-32 for TeRRa-RBS-2 are presented in Figure 7a, together with the indexed diffraction peaks based on the ICDD database. The cesium iodide diffraction pattern could be identified on those coupons except for Coupon-10 of TeRRa-RBS-1 (steam−boron effect), which agrees with the EDS mapping result (Figure 4c) that showed no CsI condensate. The diffraction intensity of cesium iodide was found to decrease at 400 K, as represented by Coupon-32 in TeRRa-RBS-1 and TeRRa-RBS-2. It was attributed to the decrease in CsI crystallite size as shown by the SEM result. This behavior had been studied by Triloki et al.[50] who showed that the decrease in CsI deposit film thickness and crystallite size resulted in the change in observable diffraction peaks, which at last led to the only (110) lattice plane ($2\theta = 27°$) observed for the 41 nm crystallite size. On Coupon-10 and Coupon-11 of TeRRa-RBS-1, the diffraction peaks of $Cs_2B_4O_7{\cdot}5H_2O$ were identified, which corroborate the Raman spectroscopic results. Cs_2CrO_4, on the other hand, has a few indexed diffraction peaks on Coupon-10 and Coupon-14 of TeRRa-RBS-2 (steam effect) due to the predominant diffractions, which resulted from CsI and stainless steel, and due partly to the crystallite size of the formed Cs_2CrO_4. Quantitative analysis on diffraction patterns that resulted from these coupons was carried out with the Rietveld refinement method using Profex version 4.3.5.[51] The refined patterns were adjusted in the diffraction angle of 20−80°. Selected diffraction patterns of TeRRa-RBS-1 and TeRRa-RBS-2 are shown in Figure 7b,c, respectively, while the overall results are summarized in Table 2. Despite the relatively low amount of Cs_2CrO_4 and $Cs_2B_4O_7{\cdot}5H_2O$ as compared to the stainless steel or CsI, we could confirm these compounds, particularly the cesium borate, in contrast to the report by Sato et al.[21] They reported that only the diffraction pattern of CsI could be identified along with the substrate of the tube. This could be caused by the difference in the selection of carrier gas (Ar with approximately 1 ppm of H_2O impurity) and the type of sampling tube material used in the study, which was made of nickel rather than stainless steel.

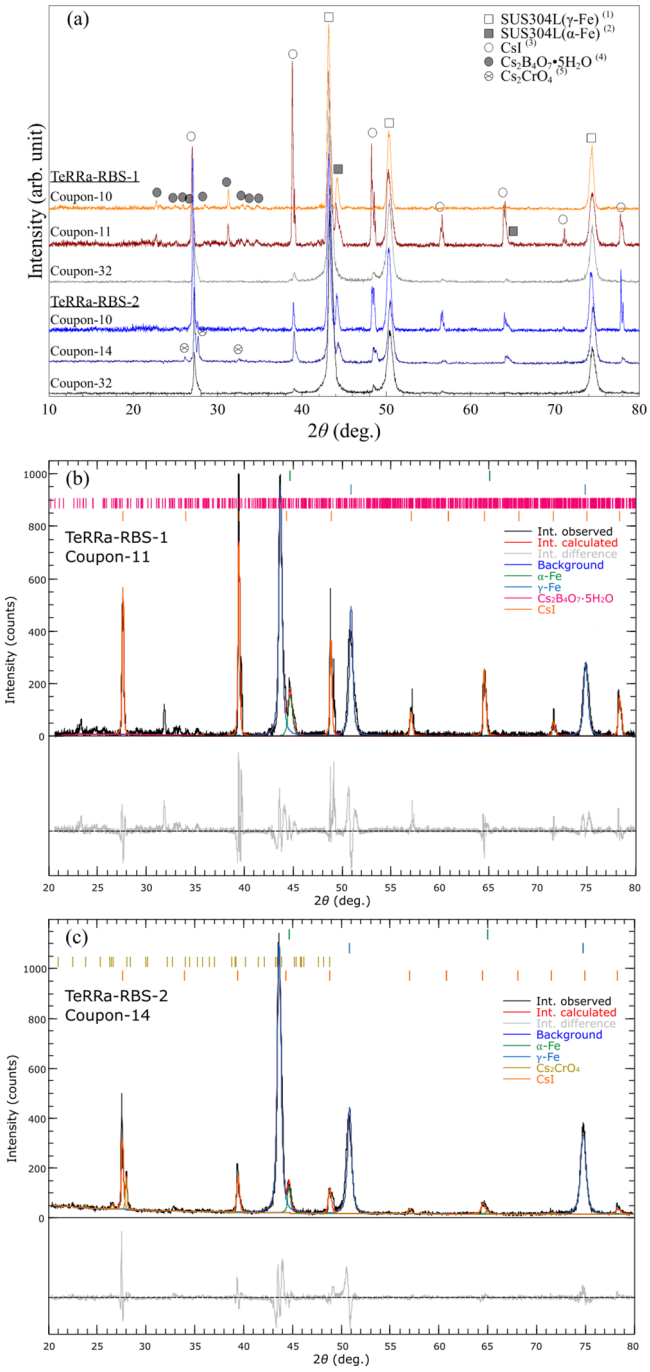

Figure 7. (a) XRD pattern of Coupon-10, Coupon-11, and Coupon-32 of TeRRa-RBS-1 and Coupon-10, Coupon-14, and Coupon-32 of TeRRa-RBS-2. ICDD card nos. (1) 71-4407, (2) 06-0696, (3) 06-0311, (4) 22-0177, and (5) 15-0748. Rietveld refinement on (b) Coupon-11 of TeRRa-RBS-1 and (c) Coupon-14 of TeRRa-RBS-1.

3.3. Thermodynamic Evaluation. *3.3.1. Steam−Boron Condition.* The dependency of boron speciation in the steam atmosphere transiting through the thermal gradient tube determines the precise mechanism of the boron−CsI interaction. In this essence, however, the present TeRRa experimental facility has not been equipped with an integrated tool for a direct determination of boron-containing species in the gas flow at a certain temperature region. As the speciation is temperature- and concentration-dependent (assuming constant total pressure), it would be estimated by (1) the B/H_2O ratio using the molar flow rate of each component and (2) evaluating the ratio in the chemical equilibrium calculation. Here, the molar flow rate of boron is defined as the vaporization rate of B_2O_3 from the alumina crucible (at 1273 K), which is, according to Krauss et al.,[25] an additive of direct

https://doi.org/10.1021/acsomega.1c04441
ACS Omega XXXX, XXX, XXX−XXX

Table 2. Quantitative Analysis of TeRRa-RBS-1 and TeRRa-RBS-2

TeRRa-RBS-1	phase (wt %)	TeRRa-RBS-2	phase (wt %)
Coupon-10	γ-Fe (88.1)	Coupon-10	γ-Fe (80.8)
	α-Fe (9.3)		α-Fe (6.3)
	CsI (−)		CsI (12.9)
	$Cs_2B_4O_7{\cdot}5H_2O$ (2.6)		Cs_2CrO_4 (−)
Coupon-11	γ-Fe (73.3)	Coupon-14	γ-Fe (90.0)
	α-Fe (8.4)		α-Fe (3.5)
	CsI (17.2)		CsI (5.1)
	$Cs_2B_4O_7{\cdot}5H_2O$ (1.1)		Cs_2CrO_4 (1.4)
Coupon-32	γ-Fe (96.9)	Coupon-32	γ-Fe (97.4)
	α-Fe (−)		α-Fe (−)
	CsI (3.1)		CsI (2.6)
	$Cs_2B_4O_7{\cdot}5H_2O$ (−)		Cs_2CrO_4 (−)

evaporation of B_2O_3 and the formation of boric acid (metaboric or orthoboric acid):

$$\dot{n}_{B_2O_3} = 3.0 \times 10^9 \exp\left(\frac{-382{,}900}{RT}\right)\frac{1}{M_{B_2O_3}} + 4.535 \cdot j_{gas} \cdot \frac{p_{H_2O}}{p_{tot}} \exp\left(\frac{-61{,}340}{RT}\right)\frac{1}{M_{acid}} \quad (2)$$

j_{gas} is the gas flow rate (g/cm^2 min), p_{H_2O} and p_{tot} are the partial pressure of H_2O and total pressure, respectively, R is the gas constant (J/mol K), T is the absolute temperature (K), M_{acid} and $M_{B_2O_3}$ are the molar mass of boric acid (as HBO_2, $(HBO_2)_3$, or H_3BO_3) and B_2O_3, respectively, in g/mol. Chemical equilibrium calculation of boron species was then calculated using Thermo-Calc 2021a with SGTE database version 5.[52] The B/H_2O ratio and stable phases estimated at 1273 K and 101.325 kPa are presented in Table 3. The Ar gas volumetric rate of 2 L/min (STP) saturated with steam at 60 °C (333 K), $\frac{p_{H_2O}}{p_{tot}}$ of 0.2, and a flow area diameter of 37.2 mm resulted in the vaporization rate of boron in a range of 1.57×10^{-7} to 4.71×10^{-7} mol/s from the alumina crucible having a cross-sectional area of 1.54×10^2 mm^2. This vaporization rate, which corresponds to B/H_2O of 5.27×10^{-4} to 1.58×10^{-3}, resulted in boric acids (HBO_2, H_3BO_3, and $(HBO_2)_3$) as the only stable phases of boron. It is worth noting that the predominant species of boron remain as metaboric acid and are followed by orthoboric acid in the gaseous phase as the concentration (B/H_2O) changes, while the trimer of metaboric acid is formed at one order fewer than the former two boron species. Nevertheless, the individual contribution of these acids to the reaction with CsI deposits (forming cesium tetraborate and cesium pentaborate) should be taken into consideration. Table 4 lists the evaluated chemical reactions of these boric acids with CsI whose products are cesium tetraborate and pentaborate and gaseous iodine. In addition, the formations of those cesium borates in a two-step reaction via cesium metaborate are also listed for the thermodynamic evaluation. The respective equilibrium constant of these reactions is provided in Table 4 after obtaining the standard Gibbs free energy of formation for each constituent.

The limited thermodynamic data of both cesium tetraborate and cesium pentaborate at high temperatures necessitate the calculation of the standard Gibbs free energy of formation based on data of chemical activity of the pseudo-binary $CsBO_2$-B_2O_3 system by Stolyarova et al.[53] using the following relations:

Table 3. Estimated Stable Phases of Boron in the Steam Atmosphere at 1273 K and 101.325 kPa

M_{acid} (g/mol)	$\dot{n}_{B_2O_3}$ [a] (g/mol)	$\dot{n}_{H_2O}$ [b] (g/mol)	B/H_2O [−]	main stable phases (mol)
43.82	4.71×10^{-7}	2.98×10^{-4}	1.58×10^{-3}	$Ar_{(g)}$ (1.67×10^{-3})
				$H_2O_{(g)}$ (4.17×10^{-4})
				$H_{2(g)}$ (7.11×10^{-7})
				$HBO_{2(g)}$ (5.02×10^{-7})
				$H_3BO_{3(g)}$ (1.25×10^{-9})
				$(HBO_2)_{3(g)}$ (1.37×10^{-8})
61.83	3.33×10^{-7}	2.98×10^{-4}	1.12×10^{-3}	$Ar_{(g)}$ (1.67×10^{-3})
				$H_2O_{(g)}$ (4.18×10^{-4})
				$HBO_{2(g)}$ (3.55×10^{-7})
				$H_3BO_{3(g)}$ (8.36×10^{-9})
				$H_{2(g)}$ (6.27×10^{-8})
				$(HBO_2)_{3(g)}$ (5.32×10^{-9})
131.5	1.57×10^{-7}	2.98×10^{-4}	5.27×10^{-4}	$Ar_{(g)}$ (1.67×10^{-3})
				$H_2O_{(g)}$ (4.18×10^{-4})
				$HBO_{2(g)}$ (5.02×10^{-7})
				$H_3BO_{3(g)}$ (1.25×10^{-9})
				$H_{2(g)}$ (1.62×10^{-8})
				$(HBO_2)_{3(g)}$ (1.37×10^{-8})

[a] Evaluated with the cross section of alumina crucible: 1.54×10^2 mm^2. [b] $\dot{n}_{H_2O}$ is calculated based on the expression $\frac{j_{gas}}{M_{H_2O}} \cdot \frac{p_{H_2O}}{p_{tot}}$ and evaluated with the flow cross section of 10.9×10^2 mm^2.

$$2CsBO_2(s) + B_2O_3(l) = Cs_2B_4O_7(s) \quad (3)$$

$$CsBO_2(s) + 2B_2O_3(l) = CsB_5O_8(s) \quad (4)$$

which at the equilibrium gives

$$\Delta_f G^\circ(Cs_2B_4O_7, s) = 2\Delta_f G^\circ(CsBO_2, s) + \Delta_f G^\circ(B_2O_3, l) - RT\{\ln(a(Cs_2B_4O_7)) - 2\ln(a(CsBO_2)) - \ln(a(B_2O_3))\} \quad (5)$$

$$\Delta_f G^\circ(CsB_5O_8, s) = \Delta_f G^\circ(CsBO_2, s) + 2\Delta_f G^\circ(B_2O_3, l) - RT\{\ln(a(CsB_5O_8)) - \ln(a(CsBO_2)) - 2\ln(a(B_2O_3))\} \quad (6)$$

Thermodynamic data of $CsBO_2$ are taken from Cordfunke et al.,[54] while data of B_2O_3 are from Barin.[55] The chemical

https://doi.org/10.1021/acsomega.1c04441
ACS Omega XXXX, XXX, XXX−XXX

Table 4. Chemical Reactions of Boric Acids with CsI and the Respective Equilibrium Constant (K_p) at 850 K

reaction[a]	K_p	reaction	K_p
$CsBO_2$			
B.1a $CsI_{(c)} + HBO_{2(g)} = CsBO_{2(c)} + HI_{(g)}$	1.34	B.1c $CsI_{(c)} + H_3BO_{3(g)} = CsBO_{2(c)} + HI_{(g)} + H_2O_{(g)}$	3.26×10^{-5}
B.1b $3CsI_{(c)} + (HBO_2)_{3(g)} = 3CsBO_{2(c)} + 3HI_{(g)}$	8.99×10^{-18}		
$Cs_2B_4O_7$		$Cs_2B_4O_7$ via B.1a–B.1c (intermediate phase $CsBO_2$)	
B.4a $2CsI_{(c)} + 4HBO_{2(g)} = Cs_2B_4O_{7(c)} + 2HI_{(g)} + H_2O_{(g)}$	2.25×10^{15}	B.4d $2CsBO_{2(c)} + 2HBO_{2(g)} = Cs_2B_4O_{7(c)} + H_2O_{(g)}$	1.25×10^{15}
B.4b $6CsI_{(c)} + 4(HBO_2)_{3(g)} = 3Cs_2B_4O_{7(c)} + 6HI_{(g)} + 3H_2O_{(g)}$	2.22×10^{-24}	B.4e $6CsBO_{2(c)} + 2(HBO_2)_{3(g)} = 3Cs_2B_4O_{7(c)} + 3H_2O_{(g)}$	2.74×10^{10}
B.4c $2CsI_{(c)} + 4H_3BO_{3(g)} = Cs_2B_4O_{7(c)} + 2HI_{(g)} + 5H_2O_{(g)}$	7.91×10^{-4}	B.4f $2CsBO_{2(c)} + 2H_3BO_{3(g)} = Cs_2B_4O_{7(c)} + 3H_2O_{(g)}$	7.43×10^{5}
CsB_5O_8		CsB_5O_8 via B.1a–B.1c (intermediate phase $CsBO_2$)	
B.5a $CsI_{(c)} + 5HBO_{2(g)} = CsB_5O_{8(c)} + HI_{(g)} + 2H_2O_{(g)}$	1.41×10^{29}	B.5d $CsBO_{2(c)} + 4HBO_{2(g)} = CsB_5O_{8(c)} + 2H_2O_{(g)}$	1.05×10^{29}
B.5b $3CsI_{(c)} + 5(HBO_2)_{3(g)} = 3CsB_5O_{8(c)} + 3HI_{(g)} + 6H_2O_{(g)}$	2.05	B.5e $3CsBO_{2(c)} + 4(HBO_2)_{3(g)} = 3CsB_5O_{8(c)} + 6H_2O_{(g)}$	2.28×10^{17}
B.5c $CsI_{(c)} + 5H_3BO_{3(g)} = CsB_5O_{8(c)} + HI_{(g)} + 7H_2O_{(g)}$	1.21×10^{6}	B.5f $CsBO_{2(c)} + 4H_3BO_{3(g)} = CsB_5O_{8(c)} + 6H_2O_{(g)}$	3.71×10^{10}

[a](c): condensed phase; (g): gas phase.

activities of cesium tetraborate and pentaborate in eqs 5 and 6 are assumed to be equal to one by taking into account the solid phase of such compounds. Consequently, data of chemical activity for both precursor materials ($CsBO_2$ and B_2O_3) derived from Stolyarova et al.[53] are limited to those below the melting temperature of $Cs_2B_4O_7$ (893 K[37]) and CsB_5O_8 (943 K[37]). The estimated data are given in Tables S1 and S2 (Supporting Information). The fitted curves on these data are plotted in Figure S1 to obtain the extrapolated data of interest for the analysis in a temperature range of 700–900 K. Further, the calculations for standard Gibbs free energy of reaction in Table 4 were carried out using the obtained data of $Cs_2B_4O_7$ and CsB_5O_8, data of CsI, H_2O, HI, HBO_2, and H_3BO_3 from Barin,[55] data of $(HBO_2)_3$ from the JANAF table,[56] and data of $CsBO_2$ from Cordfunke et al.[54]

Figure 8a presents the calculated standard Gibbs free energy of reactions of boric acids with cesium iodide. It can be

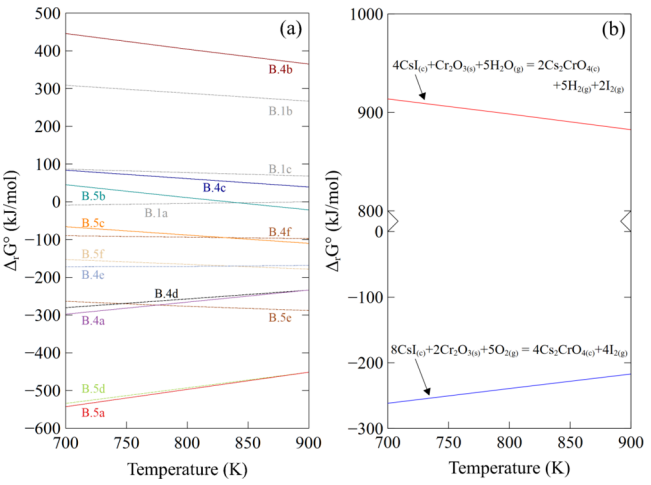

Figure 8. Standard Gibbs free energy of reaction (a) boric acids and CsI and (b) Cr_2O_3 and CsI with the carrier gas H_2O or O_2 (impurity).

classified into five groups of reactions: (I) $CsBO_2$ (reactions B.1a–B.1c); (II) $Cs_2B_4O_7$ in a one-step reaction (reactions B.4a–B.4c); (III) $Cs_2B_4O_7$ in a two-step reaction via intermediate phase $CsBO_2$ (reactions B.4d–B.4f); (IV) CsB_5O_8 in a one-step reaction (reactions B.5a–B.5c); (V) CsB_5O_8 in a two-step reaction via intermediate phase $CsBO_2$ (reactions B.5d–B.5f). Group I reactions primarily resulted in large positive values in the case of involving orthoboric acid (B.1c) and a trimer of metaboric acid (B.1b), suggesting that the intermediate phase formation is unlikely through these routes. However, for orthoboric acid, as the trend of Gibbs free energy is decreasing by the increase in temperature, the likelihood of reaction at a much greater temperature in vapor-phase reaction[57] could be high, but in the scope of our study, it is considerably unfavored.

The remaining route through metaboric acid at reaction B.1a could be possible for intermediate phase formation, considering that the obtained values were negative on a temperature lower than 900 K. That said, it was then necessary to scrutinize the equilibrium constant of this reaction. At 850 K, the mean temperature in the TGT of TeRRa-RBS-1 that showed major boron deposition (see Figure 3a), the equilibrium constant was almost unity (Table 4). This means that the reaction will not proceed to completion at the given equilibrium time as both reactants and products share the same concentration. Moreover, the EDS mapping results showed that the CsI deposits were hardly identified at this temperature, thus disproving the formation of intermediate phase $CsBO_2$. Therefore, it can be inferred that the unlikelihood of $CsBO_2$ formation consequently cancels out further reactions in the two-step reaction (B.4d–B.4f and B.5d–B.5f) despite their minima in Gibbs free energy of reaction. Further from the calculation, metaboric acid (HBO_2) was found as the only reactant to yield negative values in both groups II and IV (i.e., curve B.4a and B.5a) at all temperature ranges, which implies the favorability of such reactions. In addition, the equilibrium constants for B.4a and B.5a are much greater than those of other boric acids in the same group, indicating that the reaction process could readily proceed to completion. The orthoboric acid (H_3BO_3) yielded negative values at all temperature ranges for only group IV at reaction B.5c and potentially in a relatively higher temperature for group II at reaction B.4c. The trimer of metaboric acid was found to favor the reaction only at high temperatures for group IV (reaction B.5b). Therefore, the main chemical reactions to consider for the formation of $Cs_2B_4O_7$ and CsB_5O_8 are as follows:

$$2CsI(c) + 4HBO_2(g) = Cs_2B_4O_7(c) + 2HI(g) + H_2O(g) \quad (7)$$

$$CsI(c) + 5HBO_2(g) = CsB_5O_8(c) + HI(g) + 2H_2O(g) \quad (8)$$

$$CsI(c) + 5H_3BO_3(g) = CsB_5O_8(c) + HI(g) + 7H_2O(g) \quad (9)$$

https://doi.org/10.1021/acsomega.1c04441
ACS Omega XXXX, XXX, XXX−XXX

which also produce gaseous iodine in the form of hydrogen iodide.[19,20] In consequence, the secondary gaseous iodine observed in TeRRa-RBS-1 (Figure 3c; revaporization phase) is expected to prevail as this hydrogen iodide. The molecular iodine might also contribute to the secondary gaseous iodine upon thermal dissociation of hydrogen iodide at high temperatures.[19]

3.3.2. Steam Condition. The experimental results of TeRRa-RBS-2 have signified that the cesium chromate Cs_2CrO_4 was the condensate on the surface of stainless steel. Chemical interaction between the formed chromium oxide layer and cesium iodide deposits could not readily proceed to the formation of cesium chromate at a certain reaction temperature, but instead, it involves the carrier gas.[58]

In the following thermodynamic calculation, two plausible reactions between CsI and Cr_2O_3 were evaluated involving H_2O or O_2. The treatment of O_2 (as an impurity in the system) was considered here due to the contamination during the experiment. The source of contaminant was coming from the mixture in the upstream gas cylinder, which had contained 1 ppm of O_2. Furthermore, it was reported elsewhere[58] that the air-containing atmosphere favored the reaction between the oxidized stainless steel 304L and cesium iodide deposits. Thus, it is necessary to include such consideration in further evaluation. The chemical reactions applied in the thermodynamic calculation were as follows:

$$4CsI_{(c)} + Cr_2O_{3(s)} + 5H_2O_{(g)} = 2Cs_2CrO_{4(c)} + 5H_{2(g)} + 2I_{2(g)} \quad (10)$$

$$8CsI_{(c)} + 2Cr_2O_{3(s)} + 4O_{2(g)} = 4Cs_2CrO_{4(c)} + 4I_{2(g)} \quad (11)$$

where thermodynamic data of all constituents are from Barin,[55] except for data of Cs_2CrO_4, which were taken from Fredrickson et al.[39] Figure 8b presents the calculated standard Gibbs free energy of each reaction in the temperature of 700−900 K. The result reveals the favorability of reaction to occur only when diatomic oxygen is involved in the carrier gas, which has Δ_rG° in the range of −261 to −217 kJ/mol, in contrast with the steam effect that obtains large positive values of Δ_rG°. In other words, cesium chromate is unlikely to be formed in the pure steam atmosphere condition. This result is in agreement with the previous study conducted by Obada et al.[58] They found that the Cs-Cr compounds (i.e., Cs_2CrO_4 and $Cs_2Cr_2O_7$) were formed under an air-containing atmosphere but not under the pure steam condition through surface characterization of XPS and ToF-SIMS on stainless steel 304L after CsI deposition/revaporization. From eq 11, it is known that the product obtained from the reaction besides cesium chromate is molecular iodine. Unlike the boric acid case, molecular iodine could be directly formed without thermal dissociation of hydrogen iodide. This has a significant meaning because the species of gaseous iodine (HI or I_2) that transits to the colder location at the late phase of nuclear severe accident progression could be referred to as either the result of boric acid−CsI reactions (eqs 7−9) or oxidized stainless steel−CsI with O_2 reaction (eq 11).

Further, eq 11 shows that the inclusion of O_2 impurity will notably determine the stainless steel−CsI interaction. Thus, the partial pressure of O_2 is worth examining. At the equilibrium state, the following relation is applied:

$$\Delta_rG^\circ(\text{eq } 11) = -RT \ln \frac{p_{I_2}^4}{p_{O_2}^5} \quad (12)$$

and rearranging it will give

$$p_{O_2} = \left(p_{I_2}^4 \exp\left(\frac{\Delta_rG^\circ(\text{eq } 11)}{RT}\right)\right)^{1/5} \quad (13)$$

p_{O_2} and p_{I_2} are the partial pressure of O_2 and I_2, respectively, in Pa, Δ_rG° is the standard Gibbs free energy of reaction (J/mol), R is the gas constant (J/mol K), and T is the absolute temperature (K). As the revaporation had been elucidated to occur at the temperature of 850 K in the TGT, then one needs to first estimate the partial pressure of I_2 by assuming that the measured amount of gaseous iodine at the downstream of TGT (Figure 3c) after the second stage of heating in TeRRa-RBS-2 has resulted from such a temperature region. The measured amount of gaseous iodine from the experiment was 2.47×10^{-5} mol. Its given molar fraction will represent the partial pressure, according to Dalton's law. The other gaseous species throughout the revaporization phase (1.25 h) are Ar and H_2O, and thus, the individual amount (mol) at this period will aid in determining the molar fraction of I_2. The 2 L/min (STP) Ar-H_2O gas flow, which was saturated at 60 °C (333 K), passing through the tube with a diameter of 39.4 mm, resulted in molar flow rates of 9.77×10^{-7} mol/mm^2 s for Ar and 2.44×10^{-7} mol/mm^2 s for H_2O, which were equivalent to 5.36 mol of Ar and 1.34 mol of H_2O during the revaporization phase, respectively. Then, with the molar fraction of 3.69×10^{-6}, the partial pressure of gaseous iodine is 3.74×10^{-1} Pa. Therefore, the partial pressure of oxygen in eq 13 would be 7.14×10^{-4} Pa. This partial pressure satisfies the upper limit of impurity contained in the gas cylinder at about 1.01×10^{-1} Pa, which confirms that such a low partial pressure could induce the reaction of cesium iodide and chromium oxide layer to proceed.

4. CONCLUSIONS

Revaporization of cesium and iodide compounds from the deposits on stainless steel 304L was investigated under steam and steam−boron atmospheres. By utilizing the dedicated experimental apparatus TeRRa, solid evidence of the revaporization process had been obtained, more specifically the generation of cesium iodide aerosol and gaseous iodine. The complementary thermodynamic evaluation was conducted to further elucidate such a process and to infer appropriate main reactions. Findings in the series of experiments as well as the thermodynamic evaluation are summarized as follows:

- Most of CsI that was originally deposited in the thermal gradient tube (TGT) on a mean temperature of 850 K was found to deplete after the second heating stage with both steam and steam−boron atmospheres. The former atmosphere condition caused relative reductions of 46.0 ± 6.1% Cs and 50.9 ± 6.1% I as compared to the initial deposition, while the latter condition caused the reduction of 41.2 ± 6.2% Cs and a greater reduction of 76.1 ± 6.4% I. Depletion of cesium and a part of iodine was a result of the direct vaporization of CsI deposits, while the remaining change of iodine was caused by the chemical interactions involving the atmospheres.

https://doi.org/10.1021/acsomega.1c04441
ACS Omega XXXX, XXX, XXX−XXX

- Redeposition of CsI was then observed in both atmosphere cases on the surface of stainless steel with mean temperatures of 800 and 750 K. This influenced the amount of CsI vapor to reach the outlet of TGT (T < 400 K). The CsI that traveled to this colder location was found as aerosol.
- In the steam effect case, besides the remaining CsI deposits, cesium was found in another chemical form as cesium chromate (Cs_2CrO_4). The formation of Cs_2CrO_4 was not readily available without the inclusion of O_2 impurity in the steam flow. An oxygen partial pressure of 7.14×10^{-4} Pa was found to suffice the reaction of CsI deposits and the formed Cr_2O_3 layer on stainless steel, in which this partial pressure was below 1.01×10^{-1} Pa of O_2 in the precontained upstream gas used during the experiments. Also, the formation of cesium chromate would result in the release of gaseous molecular iodine (I_2) based on the reaction $8CsI_{(c)} + 2Cr_2O_{3(s)} + 5O_{2(g)} = 4Cs_2CrO_{4(c)} + 4I_{2(g)}$.
- In the steam−boron effect case, gaseous metaboric acid (HBO_2) and, to a lesser extent, the orthoboric acid (H_3BO_3) were found as the stable phases in the B_2O_3-H_2O system at our laboratory-scale experiment. These boric acids interacted with CsI deposits and caused formations of dicesium tetraborate pentahydrate ($Cs_2B_4O_7{\cdot}5H_2O$) and cesium pentaborate tetrahydrate ($CsB_5O_8{\cdot}4H_2O$). Thermodynamic calculation suggested that these cesium borates were formed by direct reaction of CsI deposits with either HBO_2 or H_3BO_3 and not by indirect reactions via an intermediate phase of cesium metaborate ($CsBO_2$). Subsequently, gaseous iodine in the form of hydrogen iodide (HI) was released from such reactions. The main chemical reactions are as follows:

$$2CsI(c) + 4HBO_2(g) = Cs_2B_4O_7(c) + 2HI(g) + H_2O(g)$$

$$CsI(c) + 5HBO_2(g) = CsB_5O_8(c) + HI(g) + 2H_2O(g)$$

$$CsI(c) + 5H_3BO_3(g) = CsB_5O_8(c) + HI(g) + 7H_2O(g)$$

Unlike the steam effect case, which highly depended on the contained O_2 in the gas flow that might limit the amount of cesium chromate and thus gaseous iodine to form, the steam−boron case—considering the abundance of boric acids in the system—was able to generate cesium borates in a larger amount, which consequently could release larger gaseous iodine (as hydrogen iodide) than what the steam case could release.

The results in this study have unveiled how each steam atmospheric condition, in the presence or absence of boron, caused a distinct interaction mechanism with CsI deposits. Chemical reactions obtained from thermodynamic evaluation were of great importance to be implemented in the ECUME database and therefore made them pertinent for analysis in SA codes.

In the event of a nuclear severe accident, the composition of gaseous species is dynamically changed based on the accident progression scenario, and the interaction of these gaseous species with cesium iodide will be important to assess both the form and volatility of iodine under such conditions. We demonstrated in this study that after cesium iodide had been released and then deposited on the structural material of the reactor coolant system (RCS) such as stainless steel, the late-phase steam- and boric acid-containing gas flow could chemically interact with it. Their particular interactions led to the release of gaseous iodine either as molecular iodine (I_2) when the steam (with a fractional amount of O_2) was in the gaseous species or as hydrogen iodide (HI) when boric acids were involved. The volatility of this gaseous iodine that was able to reach a lower temperature location (T < 400 K) could indicate a significance to affect the containment atmosphere. Therefore, the respective form of such gaseous iodine measured/detected in any specific locations at the later stage of accident progression determines its origin in either mechanism. Our findings have also signified that those mechanisms should be considered for the comprehension of evaluating the gaseous iodine release, in addition to the past work analyzing the release of molecular iodine from the reaction between semivolatile materials Mo and CsI.[59] Apart from the gaseous iodine, cesium will mainly be revaporized as CsI, yet some part of cesium will be retained in the RCS in the form of low volatile cesium chromate or cesium borates.

■ ASSOCIATED CONTENT

Supporting Information

The Supporting Information is available free of charge at https://pubs.acs.org/doi/10.1021/acsomega.1c04441.

Supporting text containing the estimated standard Gibbs energy of formation of $Cs_2B_4O_7$ and CsB_5O_8 based on pseudo-binary activity data of $CsBO_2$-B_2O_3 (PDF)

■ AUTHOR INFORMATION

Corresponding Author

Muhammad Rizaal − *Nuclear Science and Engineering Center, Japan Atomic Energy Agency, Tokai-mura, Ibaraki 319-1195, Japan*; orcid.org/0000-0003-2198-2325; Email: rizaal.muhammad@jaea.go.jp

Authors

Shuhei Miwa − *Nuclear Science and Engineering Center, Japan Atomic Energy Agency, Tokai-mura, Ibaraki 319-1195, Japan*

Eriko Suzuki − *Nuclear Science and Engineering Center, Japan Atomic Energy Agency, Tokai-mura, Ibaraki 319-1195, Japan*

Junpei Imoto − *Nuclear Science and Engineering Center, Japan Atomic Energy Agency, Tokai-mura, Ibaraki 319-1195, Japan*

Masahiko Osaka − *Nuclear Science and Engineering Center, Japan Atomic Energy Agency, Tokai-mura, Ibaraki 319-1195, Japan*

Mélany Gouëllo − *VTT Technical Research Centre of Finland, Espoo FI-02044 VTT, Finland*

Complete contact information is available at: https://pubs.acs.org/10.1021/acsomega.1c04441

Notes

The authors declare no competing financial interest.

■ ACKNOWLEDGMENTS

This work was done in the framework of collaboration between JAEA and VTT under the support of the Academy of Finland (grant number 294995). The authors express sincere gratitude

to Dr. Kunihisa Nakajima for the fruitful discussion on thermodynamic calculation, Mr. Juntaro Takada and Mr. Kunihiro Sumiya for the technical support on the TeRRa facility, and Mr. Akinori Yamaguchi for the technical support on Raman spectroscopy. Thanks are also due to Dr. Yoshiyuki Nemoto and Dr. Chikashi Suzuki for feedbacks on the preparation of the manuscript.

REFERENCES

(1) Klein-Heßling, W.; Sonnenkalb, M.; Jacquemain, D.; Clément, B.; Raimond, E.; Dimmelmeier, H.; Azarian, G.; Ducros, G.; Journeau, C.; Puebla, L. E. H.; Schumm, A.; Miassoedov, A.; Kljenak, I.; Pascal, G.; Bechta, S.; Güntay, S.; Koch, M. K.; Ivanov, I.; Auvinen, A.; Lindholm, I. Conclusions on severe accident research priorities. *Ann. Nucl. Energy* **2014**, *74*, 4−11.

(2) Suehiro, S.; Sugimoto, J.; Hidaka, A.; Okada, H.; Mizokami, S.; Okamoto, K. Development of the source term PIRT based on findings during Fukushima Daiichi NPPs accident. *Nucl. Eng. Des.* **2015**, *286*, 163−174.

(3) Schwinges, B.; Journeau, C.; Haste, T.; Meyer, L.; Tromm, W.; Trambauer, K. Ranking of severe accident research priorities. *Prog. Nucl. Energy* **2010**, *52*, 11−18.

(4) Sehgal, B. R. Accomplishments and challenges of the severe accident research. *Nucl. Eng. Des.* **2001**, *210*, 79−94.

(5) Gauntt, R.O.; Cole, R. K.; Erickson, C. M.; Gido, R. I. G.; Gasser, R. D.; Rodriguez, S. B.; Young, M. F. MELCOR computer code manuals: primer and user's guide version 1.8.5. *NUREG/CR-6119*; Sandia National Laboratories: Albuquerque, CA, 2005.

(6) Matsumoto, T.; Ishikawa, J.; Maruyama, Y. Analysis for progression of accident at Fukushima Dai-ichi nuclear power station with THALES2 code. *Proceeding of 16th International Topical Meeting on Nuclear Reactor Thermal Hydraulics (NURETH)*; Chicago (US), August 30−September 4, 2015, pp. 4033−4043.

(7) Sonnenkalb, M.; Pellegrini, M.; Herranz, L. E.; Lind, T.; Morreale, A. C.; Kanda, K.; Tamaki, H.; Kim, S. I.; Cousin, F.; Fernandez Moguel, L.; Andrews, N.; Sevon, T. Overview and outcomes of the OECD/NEA benchmark study of the accident at the Fukushima Daiichi NPS (BSAF), phase 2 − Results of severe accident analyses for unit 2. *Nucl. Eng. Des.* **2020**, *369*, 110840.

(8) Herranz, L. E.; Pellegrini, M.; Lind, T.; Sonnenkalb, M.; Godin-Jacqmin, L.; López, C.; Dolganov, K.; Cousin, F.; Tamaki, H.; Kim, T. W.; Hoshi, H.; Andrews, N.; Sevon, T. Overview and outcomes of the OECD/NEA benchmark study of the accident at the Fukushima Daiichi NPS (BSAF) Phase 2 − Results of severe accident analyses for Unit 1. *Nucl. Eng. Des.* **2020**, *369*, 110849.

(9) Miwa, S.; Yamashita, S.; Ishimi, A.; Osaka, M.; Amaya, M.; Tanaka, K.; Nagase, F. Research program for the evaluation of fission product and actinide release behaviour, focusing on their chemical forms. *Energy Procedia* **2015**, *71*, 168−181.

(10) Miwa, S.; Takase, G.; Imoto, J.; Nishioka, S.; Miyahara, N.; Osaka, M. Boron chemistry during transportation in the high temperature region of a boiling water reactor under severe accident conditions. *J. Nucl. Sci. Technol.* **2020**, *57*, 291−300.

(11) Osaka, M.; Miwa, S.; Nakajima, K.; Di Lemma, F. G.; Suzuki, C.; Miyahara, N.; Kobata, M.; Okane, T.; Suzuki, E. *Results and progress of fundamental research on fission product chemistry − Progress report in 2015*; JAEA-Review 2016−026; Japan Atomic Energy Agency: Ibaraki, Japan. 2016, DOI: 10.11484/jaea-review-2016-026.

(12) Di Lemma, F. G.; Nakajima, K.; Yamashita, S.; Osaka, M. Surface analyses of cesium hydroxide chemisorbed onto type 304 stainless steel. *Nucl. Eng. Des.* **2016**, *305*, 411−420.

(13) Di Lemma, F. G.; Yamashita, S.; Miwa, S.; Nakajima, K.; Osaka, M. Prediction of chemical effects of Mo and B on the Cs chemisorption onto stainless steel. *Energy Procedia* **2017**, *127*, 29−34.

(14) Suzuki, E.; Nakajima, K.; Osaka, M. Effect of atmosphere on the vaporization behavior of $CsFeSiO_4$. *Prog. Nucl. Sci. Technol.* **2018**, *5*, 165−167.

(15) Nishioka, S.; Nakajima, K.; Suzuki, E.; Osaka, M. An experimental investigation of influencing chemical factors on Cs-chemisorption behavior onto stainless steel. *J. Nucl. Sci. Technol.* **2019**, *56*, 988−995.

(16) Miyahara, N.; Miwa, S.; Gouëllo, M.; Imoto, J.; Horiguchi, N.; Sato, I.; Osaka, M. Experimental study on transport behavior of cesium iodide in the reactor coolant system under LWR severe accident conditions. *J. Nucl. Sci. Technol.* **2020**, *57*, 1287−1296.

(17) Miyahara, N.; Miwa, S.; Horiguchi, N.; Sato, I.; Osaka, M. Chemical reaction kinetics dataset of Cs-I-B-Mo-O-H system for evaluation of fission product chemistry under LWR severe accident conditions. *J. Nucl. Sci. Technol.* **2019**, *56*, 228−240.

(18) Miwa, S.; Nakajima, K.; Miyahara, N.; Nishioka, S.; Suzuki, E.; Horiguchi, N.; Liu, J.; Miradji, F.; Imoto, J.; Mohamad, A.; Takase, G.; Karasawa, H.; Osaka, M. Development of fission product chemistry database ECUME for the LWR severe accident. *Mech. Eng. J.* **2020**, *7*, 19−00537.

(19) Bowsher, B. R.; Nichols, A. L. *High-temperature studies of simulant fission products. Part IV: Interaction of caesium iodide with boric acid over the temperature range 400 to 1000°C; AEEW-R 1973*; United Kingdom Atomic Energy Establishment, Winfrith, United Kingdom. 1985.

(20) Bowsher, B. R.; Dickinson, S. *The interaction of caesium iodide with boric acid: Vapour phase and vapour-condensed phase reactions; AEEW-R 2102*; United Kingdom Atomic Energy Establishment, Winfrith, United Kingdom, Report. 1986.

(21) Sato, I.; Onishi, T.; Tanaka, K.; Iwasaki, M.; Koyama, S. Influence of boron vapor on transport behavior of deposited CsI during heating test simulating a BWR severe accident condition. *J. Nucl. Mater.* **2015**, *461*, 22−28.

(22) Gouëllo, M.; Hokkinen, J.; Kärkelä, T.; Auvinen, A. A scoping study of the chemical behavior of cesium iodide in the presence of boron in the condensed phase (650°C and 400°C) under primary circuit conditions. *Nucl. Technol.* **2018**, *203*, 66−84.

(23) Minato, K. Thermodynamic analysis of cesium and iodine behavior in severe light water reactor accidents. *J. Nucl. Mater.* **1991**, *185*, 154−158.

(24) Girault, N.; Payot, F. Insights into iodine behaviour and speciation in the Phébus primary circuit. *Ann. Nucl. Energy* **2013**, *61*, 143−156.

(25) Krauss, W.; Schanz, G.; Steiner, H. *Tg-rig tests (thermal balance) on the oxidation of B4C; FZKA 6883*; Forschungszentrum Karlsruhe GmbH, Karlsruhe, Germany. 2003.

(26) Kurata, M.; Barrachin, M.; Haste, T.; Steinbrueck, M. Phenomenology of BWR fuel assembly degradation. *J. Nucl. Mater.* **2018**, *500*, 119−140.

(27) Housiadas, M.; Kissane, M.; Sehgal, B. R. Fission Product Release and Transport. In *Nuclear safety in light water reactors*; Sehgal, B. R., Ed., Academic Press: New York: 2012; pp. 425−517, DOI: 10.1016/B978-0-12-388446-6.00005-8.

(28) Elrich, R. M.; Sallach, R. A.; Oulette, A. L.; Douglas, S. C. *Reaction between some cesium-iodine compounds and the reactors materials 304 stainless steel, Inconel 600 and silver. Volume 1: cesium hydroxide reactions*; NUREG/CR-3197-VOL.1; Sandia National Laboratory: Albuquerque, CA. 1984.

(29) Ishida, T.; Harayama, Y.; Yaguchi, S. Oxidation of 304 stainless steel in high-temperature steam. *J. Nucl. Mater.* **1986**, *140*, 74−84.

(30) Mamede, A. S.; Nuns, N.; Cristol, A. L.; Cantrel, L.; Souvi, S.; Cristol, S.; Paul, J. F. Multitechnique characterisation of 304L surface states oxidised at high temperature in steam and air atmospheres. *Appl. Surf. Sci.* **2016**, *369*, 510−519.

(31) Steinbrück, M.; Veshchunov, M. S.; Boldyrev, A. V.; Shestak, V. E. Oxidation of B4C by steam at high temperatures: New experiments and modelling. *Nucl. Eng. Des.* **2007**, *237*, 161−181.

(32) Berlin, J. Analysis of boron with energy dispersive X-ray spectrometry: Advances in Light Element Analysis with SDD Technology. *Imaging Microsc.* **2011**, *13*, 19−21.

https://doi.org/10.1021/acsomega.1c04441
ACS Omega XXXX, XXX, XXX−XXX

(33) Ingemarsson, L.; Halvarsson, M. *SEM/EDX Analysis of Boron*; High Temperature Corrosion Centre (HTC), Chalmers University of Technology. 2011.
(34) Cordfunke, E. H. P.; Prins, G.; et al. *Thermochim. Acta* **1985**, *90*, 169−176.
(35) Hidaka, A.; Igarashi, M.; Hashimoto, K.; Sato, H.; Yoshino, T.; Sugimoto, J. Experimental and analytical study on the behavior of cesium iodide aerosol/vapor deposition onto inner surface of pipe wall under severe accident conditions. *J. Nucl. Sci. Technol.* **1995**, *32*, 1047−1053.
(36) Cordfunke, E. H. P. Thermodynamic properties of CsI. II. vapour pressures and thermochemical properties of CsI(g) and Cs_2I_2(g). *Thermochim. Acta* **1986**, *108*, 45−55.
(37) Penin, N.; Touboul, M.; Nowogrocki, G. New form of the Cs2O−B2O3 phase diagram. *J. Cryst. Growth* **2003**, *256*, 334−340.
(38) Vandeputte, R.; Khiri, D.; Lafont, C.; Cantrel, L.; Louis, F. Theoretical investigation of thermochemical properties of cesium borates species. *J. Nucl. Mater.* **2019**, *517*, 63−70.
(39) Fredrickson, D. R.; Johnson, G. K.; O'Hare, P. A. G. Cesium chromate, Cs_2CrO_4: high-temperature enthalpy increments and other thermodynamic properties. *J Chem. Thermodyn.* **1980**, *12*, 801−805.
(40) Haste, T.; Payot, F.; Dominguez, C.; March, P.; Simondi-Teisseire, B.; Steinbrück, M. Study of boron behaviour in the primary circuit of water reactors under severe accident conditions: A comparison of Phebus FPT3 results with other recent integral and separate-effects data. *Nucl. Eng. Des.* **2012**, *246*, 147−156.
(41) Allen, G. C.; Bowsher, B. R.; Dickinson, S.; Fotios, G. M.; Nichols, A. L.; Wild, R. K. *High temperature studies of simulant fission products: Part VI, Surface studies of the interaction of caesium hydroxide vapour with 304 stainless steel; AEEW-R 86*; United Kingdom Atomic Energy Establishment: Winfrith, United Kingdom, 1985.
(42) Lixia, Z.; Tao, Y.; Jiang, W.; Shiyang, G. FT-IR and Raman spectroscopic study of hydrated rubidium (cesium) borates and alkali double borates. *Russ. J. Inorg. Chem.* **2007**, *52*, 1786−1792.
(43) Zhihong, L.; Bo, G.; Mancheng, H.; Shuni, L.; Shuping, X. FT-IR and Raman spectroscopic analysis of hydrated cesium borates and their saturated aqueous solution. *Spectrochim. Acta A* **2003**, *59*, 2741−2745.
(44) Touboul, M.; Penin, N.; Nowogrocki, G. Crystal Structure and Thermal Behavior of Cs2[B4O5(OH)4]3H2O. *J. Solid State Chem.* **1999**, *143*, 260−265.
(45) Penin, N.; Seguin, L.; Gerand, B.; Touboul, M.; Nowogrocki, G. Crystal structure of a new form of $Cs[B_5O_6(OH)_4]$. $2H_2O$ and thermal behavior of $M[B_5O_6(OH)_4].2H_2O$ (M=Cs, Rb, Tl). *J. Alloys Compd.* **2002**, *334*, 97−109.
(46) Anderson, Y. E.; Filatov, S. K.; Polyakova, I. G.; Bubnova, R. S. Thermal behavior of $M^+B_5O_6(OH)_4{\cdot}2H_2O$ (M^+ = K, Rb, Cs) and polymorphic transformations of CsB_5O_8. *Glass Phys. Chem.* **2004**, *30*, 450−460.
(47) Carter, R. L.; Bricker, C. E. Laser-raman spectra of crystalline K_2CrO_4, Rb_2CrO_4 and Cs_2CrO_4. *Spectrochim. Acta A* **1971**, *27*, 569−580.
(48) Kovács, A.; Konings, R. J. M. Molecular data of mixed metal oxides with importance in nuclear safety. *J. Nucl. Mater.* **2016**, *477*, 134−138.
(49) McCarty, K. F.; Boehme, D. R. A raman study of the systems $Fe_{3-x}Cr_xO_4$ and $Fe_{2-x}Cr_xO3$. *J. Solid State Chem.* **1989**, *79*, 19−27.
(50) Triloki; Garg, P.; Rai, R.; Singh, B. K. Structural characterization of as-deposited cesium iodide films studied by X-ray diffraction and transmission electron microscopy techniques. *Nucl. Instrum. Methods Phys. Res. A* **2014**, *736*, 128−134.
(51) Doebelin, N.; Kleeberg, R. Profex: A graphical user interface for the rietveld refinement program BGMN. *J. Appl. Crystallogr.* **2015**, *48*, 1573−1580.
(52) Andersson, J.-O.; Helander, T.; Höglund, L.; Shi, P.; Sundman, B. Thermo-Calc and DICTRA, Computational tools for materials science. *Calphad* **2002**, *26*, 273−312.
(53) Stolyarova, V. L.; Vorozhtcov, V. A.; Lopatin, S. I.; Shugurov, S. M.; Simonenko, E. P.; Simonenko, N. P.; Masaki, K.; Costa, D. High temperature mass spectrometric study of vaporization and thermodynamics of the Cs_2O-B_2O_3 system: Review and experimental investigation. *Rapid Commun. Mass Spectrom.* **2021**, *35*, No. e9079.
(54) Cordfunke, E. H. P.; Konings, R. J. M.; Westrum, E. F., Jr. The thermodynamic properties of cesium metaborate $CsBO_2$ from 5 to 1000 K. *Thermochim. Acta* **1988**, *128*, 31−38.
(55) Barin, I. *Thermochemical data of pure substances*; 3rd ed.; VCH Verlagsgesellschaft mbH: Weinheim, Germany. 1995, DOI: 10.1002/9783527619825.
(56) *NIST-JANAF thermochemical tables*; 4th ed,; Part I Al−Co. American Institute of Physics: (accessed 2021-01-28).
(57) Nakajima, K.; Takai, T.; Furukawa, T.; Osaka, M. Thermodynamic study of gaseous $CsBO_2$ by Knudsen effusion mass spectrometry. *J. Nucl. Mater.* **2017**, *491*, 183−189.
(58) Obada, D.; Mamede, A. S.; Nuns, N.; Grégoire, A. C.; Gasnot, L. Combined ToF-SIMS and XPS characterization of 304L surface after interaction with caesium iodide under PWR severe accident conditions. *Appl. Surf. Sci.* **2018**, *459*, 23−31.
(59) Gouëllo, M.; Hokkinen, J.; Kärkelä, T. Advances in the understanding of molybdenum effect on iodine and caesium reactivity in condensed phase in the primary circuit in nuclear severe accident conditions. *Nucl. Eng. Technol.* **2020**, *52*, 1638−1649.

https://doi.org/10.1021/acsomega.1c04441
ACS Omega XXXX, XXX, XXX−XXX